This is a preprint, the final version is subject to change, of the American Mineralogist (MSA)
Cite as Authors (Year) Title. American Mineralogist, in press.
DOI: https://doi.org/10.2138/am-2018-6524

Revision 1

Sn-Isotope Fractionation as a Record of Hydrothermal Redox Reactions

Junming Yao[1], Ryan Mathur[2]*, Wayne Powell[3], Bernd Lehmann[4], Fernando Tornos[5], Marc Wilson[6], Joaquin Ruiz[7]

1. Key Laboratory of Mineralogy and Metallogeny, Guangzhou Institute of Geochemistry, Chinese Academy of Sciences, Guangzhou. China

2. Juniata College, Huntingdon PA, USA *

3. Brooklyn College, City University of New York, Brooklyn NY, USA

4. Mineral ResourcesTechnical University of Clausthal, Clausthal-Zellerfeld, Germany

5. Instituto de Geociencias (CSIC-UCM), Madrid, Spain

6. Carnegie Museum of Natural History, Pittsburgh PA, USA

7. University of Arizona, Tucson AZ, USA

*corresponding author

Abstract

A redox reaction in which reduced Sn^{2+} oxidizes to Sn^{4+} is thought to occur during the precipitation of cassiterite (SnO_2) and stannite (Cu_2FeSnS_4) from high-temperature hydrothermal solutions. In four stanniferous regions with differing mineralization environments (South Dakota, USA; Cornwall, England; Erzgebirge, Germany/Czech Republic; Andean tin belt, Bolivia), the tin isotope composition in stannite (mean value $\delta^{124}Sn$=-1.47±0.54‰, n=21) is consistently more fractionated toward negative values than that of paragenetically-earlier cassiterite (mean value $\delta^{124}Sn$=0.48±0.62‰, n=50). Given the oxidation-dependent mechanism for cassiterite precipitation, this isotopic shift is most likely attributable to the oxidation of Sn in solution; precipitation of heavy-Sn-enriched cassiterite results in residual dissolved Sn with lighter isotopic composition, which is expressed in the negative $\delta^{124}Sn$ values of later-formed stannite. Equally important is that the mean values for the cassiterite from the various deposits are slightly different and may indicate that the initial Sn isotope composition in early formed cassiterite relates to variations in the source or magmatic processes. Therefore, the tin isotopes hold potential to provide information on both redox geochemical reactions and petrologic source or process.

Introduction

Tin has been an economically significant metal since it was first alloyed with copper to produce bronze nearly 7000 years ago (Radivojevic et al., 2013). Tin exhibits complex behavior, acting as a volatile, siderophile, and chalcophile element, and may exist in the Sn^0, Sn^{2+}, or Sn^{4+} valence state. Although it is rare, with an average crustal abundance of 1.7ppm (Rudnick and Gao, 2003), it has the largest number of naturally formed isotopes (10) and exhibits the greatest mass range (112-124 amu) of any element on the periodic table. Given that the degree of isotopic fractionation is related, in part, to the relative mass difference of the isotopes, the large mass range of Sn may allow for the monitoring of fractionation of a heavy metal that is typically associated with hydrothermal systems related to felsic magmatism (Lehmann, 1990).

Measurable isotopic fractionation of tin has been reported for ores (Haustein et al., 2010), igneous rocks (Creech et al., 2017; Badullovich et al., 2017), and archaeological bronze

artifacts (Balliana et al., 2013; Yamazaki et al., 2014; Mason et al., 2016). The isotopic variation measured in these materials indicates that high-temperature geological processes fractionate tin isotopes. Only Badullovich et al. (2017) has presented evidence for an associated mechanism that induces isotopic variation of tin—partitioning of Sn^{4+} between magma and ilmenite during fractional crystallization of basalt. However, no studies have focused on the processes and materials associated with tin mineralization: highly evolved felsic magmas, involvement of a saline hydrothermal fluid, rapidly evolving redox conditions, and distinct mineral assemblages in which cassiterite (SnO_2) is predominant. Without an understanding of causative mechanisms of fractionation in typical hydrothermal tin ore systems, interpretation of Sn isotopic data by geologists and archaeologists is limited.

Tin experiences electron transfer in high-temperature geochemical reactions, including those associated with the precipitation of cassiterite in tin mineralizing systems (Eugster, 1985). The precipitation of cassiterite is likely dominated by the reactions associated with the oxidation of Sn-chloride complexes, such as:

$Sn^{2+}Cl_x^{2-x} + 2H_2O = Sn^{4+}O_2 + 2H^+ + xCl^- + H_2$ (Heinrich, 1990), and

$SnCl_3^- + H^+ + 2H_2O = SnO_2 + 3HCl + H_2$ (Korges et al, 2018).

Based on fluid inclusion analysis and mineral stability studies, cassiterite precipitation from hydrothermal solutions can occur across a wide temperature range (320-550°C), although the main phase of cassiterite precipitation in most ores typically occurs within the temperature range of approximately 400-350°C (Campbell and Panter, 1990; Markl and Schumacher, 1996; Korges et al., 2018).

Redox reactions are known to fractionate isotopes in numerous metal systems (e.g., Cu, Fe). Furthermore, inelastic nuclear resonant X-ray scattering (INRXS) and Mössbauer spectroscopy experiments predict that oxidation state has a large effect on fractionation of Sn (from δ^{122}Sn=0.4 to 4.1 per mil for Sn^{+2} and Sn^{+4} species) within the range of temperatures associated with tin mineralization (300-700°C) (Polyakov et al., 2005). Thus, fractionation associated with oxidation may account for much of the observed isotopic variation in this metal. Accordingly, the purpose of this study is to empirically evaluate and model the role of redox reactions as a mechanism for Sn isotope fractionation in association with hydrothermal processes by comparing Sn isotope values for paragenetically early and late tin minerals. The

early formation of cassiterite and the late formation of stannite in hydrothermal systems is well established from detailed ore microscopy work on classical tin provinces (Cornwall: Jackson et al., 1982; Bolivia: Kelly and Turneaure, 1970; Spain: Chicharro et al., 2016).

Rationale for Redox Reactions as a Mechanism for Sn Isotope Fractionation

In well-studied multi-valent transition metal isotopic systems such as Cu and Fe, it has been established that redox reactions impart significant fractionation, with oxidation favoring the heavier isotope in low temperature reactions (Zhu, 2002; Borrok et al., 2008; Pokrovsky et al., 2008; Mathur et al., 2010). Given that Sn undergoes a redox reaction in hydrothermal fluids during mineralization, it is likely that the electron transfer required for the formation of cassiterite or soluble Sn^{4+}-complexes will favor the heavier isotopes of tin.

The solubility of tin in granitic magmas is redox dependent. Experimental studies have demonstrated that under reducing conditions, where tin exists predominantly in the Sn^{2+} state, cassiterite solubility is orders of magnitude greater than under oxidizing conditions where Sn^{4+} is the dominant stable species (Linnen et al., 1995, 1996). Oxygen fugacity values for tin granites lie between the QFM and NNO buffer, allowing for high dissolved Sn^{2+} contents (Heinrich et al., 1990) that become further concentrated in differentiated water- and halogen-rich residual magmas (Lehmann, 1982). In addition, Linnen et al. (1996) concluded that peraluminous granites have a greater Sn^{2+}/Sn^{4+} ratio than that of other granite compositions. Subsequent work demonstrated that the dominance of Sn^{2+} in peraluminous granites persists over a wide range of redox conditions (QFM to QFM +2.4) (Farges et al., 2006).

Due to the redox and compositional dependence of Sn solubility in granitic magmas, primary Sn-mineralization is associated with ilmenite-series granites, typically peraluminous that derive their low fO_2 character from the partial melting of organic-bearing sedimentary rocks (Lehmann, 1982; Černý et al., 2005). At shallow crustal levels, tin will partition to exsolved aqueous hydrothermal fluids, predominantly as Sn^{2+}-chloride complexes (Eugster, 1985).

Cassiterite (SnO_2) is the primary economic tin mineral, and its precipitation from reduced, magma-derived hydrothermal fluids requires electron transfer to produce Sn^{4+}. Possible triggers for oxidation of hydrothermal fluids include mixing with meteoric waters, pH

change due to progressive hydrolysis (greisen development), or vapor separation (e.g., Heinrich, 1990). Oxidation of tin within peraluminous magma may also result in cassiterite nucleation because Sn^{4+} cannot be accommodated in the melt structure (Farges et al., 2006). Regardless of the specific process and site associated with mineralization, redox reactions are essential to the genesis of all primary cassiterite ores.

Tin in Minerals, Granites and Ores

Recent direct U-Pb dating of hydrothermal cassiterite and U-Pb zircon ages of associated granite have confirmed the coeval timing of hydrothermal mineralization with late-stage granite magmatism (Yuan et al., 2011; Chen et al., 2014; Zhang et al, 2015, 2017). Ore is spatially associated with apical positions of cupolas that are composed of the latest-stage differentiates of larger bodies of tin granite, and in which Sn-enriched volatiles accumulate (e.g., Groves, 1972; Plimer, 1987). If the magma is emplaced at sufficiently shallow depths, ultimately, hydrothermal brines are released by hydraulic fracturing of the granitic carapace (Plimer, 1987).

Ores associated with tin granites commonly exhibit a mineralogical zoning pattern where tin, in the form of cassiterite, is concentrated proximal to the granite contact, whereas Cu-Pb-Zn sulfide ores form at greater distance or overprint earlier cassiterite in proximal parts of the system. Tin in sulfides is usually in low abundance, most commonly in the form of stannite (Cu_2FeSnS_4), and forms later in the paragenetic sequence compared to cassiterite (Sillitoe et al., 1975; Sugaki et al., 1981; Lehmann 1987, Chicharro et al., 2016). Tin is present in the Sn^{4+} state in both cassiterite and stannite, with the cation valences in stannite being $Cu^{+}{}_2Fe^{2+}Sn^{4+}S_4$ (Eibschütz et al. 1967; Greenwood and Whitfield, 1968).

Early cassiterite precipitation results from oxidation, either associated with hydrolysis of feldspars (greisenization) or mixing with meteoric waters (Heinrich, 1990; Heinrich and Ryan, 1992; Chicharro et al., 2016). Late stage Sn-sulfide assemblages precipitate due to pressure and temperature decrease associated with higher-level hydraulic fracturing, further mixing with meteoric water, and further oxidation due to the liberation of H_2 vapor (Heinrich and Ryan, 1992; Chicharro et al., 2016). This mixing provides an additional source of reduced sulfur, cools and dilutes the hydrothermal brine, but does not introduce additional Sn (Heinrich and Ryan,

1992). Thus, each hydrothermal tin mineralizing system is associated with a single, localized Sn source (highly differentiated granite), and a single magmatic-hydrothermal fluid (Korges et al., 2018); this fluid undergoes progressive oxidation during its ascent. If oxidation favors the heavier isotopes of Sn, then cassiterite precipitation would leave the remaining Sn^{2+} in solution enriched in the lighter isotopes. Within an ore deposit this isotopic shift would be expected to be recorded in the contrasting Sn isotope composition of the paragenetically earlier cassiterite (heavy isotope enriched) and late-stage stannite (light isotope enriched).

Isolating the contribution of redox reactions to Sn fractionation may be impeded by overprints associated with additional fractionation mechanisms. Sn^{4+} may substitute for Ti in a variety of oxides and silicates, potentially resulting in isotopic partitioning between coexisting mineral phases. In tin granites biotite may contain as much as 1000 ppm Sn (Neiva, 1976; Imeokparia, 1982; Wang et al., 2013). Titanite ($CaTiSiO_5$) and malayaite ($CaSnSiO_5$) form a solid solution. Near end-member malayaite has been documented in Sn-skarns from New South Wales (Plimer, 1984), and titanite with as much as 26 wt% SnO_2 has been reported from granites in southern China (Xie et al., 2010; Wang et al., 2013). Other Sn-bearing minerals in skarns and granites include garnet, clinopyroxene, magnetite, and rutile (Plimer, 1984; Wang et al., 2013). Given the complexity of Sn-bearing mineral assemblages in both granites and skarns, this study emphasizes the mineralogically simpler ores associated with veins and greisens within silicate host rocks.

Tin deposits display considerable variation but can be classified based on their relative depth, position relative to the granite contact, and style of mineralization (Taylor, 1979). Herein, we examine classic localities from four distinct styles of tin mineralization (Fig. 1):

1) Deposits associated with batholithic magmatic environments (e.g., Erzgebirge) in which extensive quartz-muscovite-topaz replacement (greisenization) with disseminated cassiterite is predominant over large-scale veining, and the majority of mineralization lies within, or immediately above, granite cupolas. At Cinovec (Zinnwald) in the Erzgebirge, cassiterite ore is hosted predominantly by greisens formed under lithostatic pressures, with lesser ore within approximately coeval veins that developed under hydrostatic conditions at a depth of 2-3 km and at temperatures between 335 and 410°C (Korges et al., 2018).

2) Deposits associated with granitoids of deep subvolcanic character (e.g., Cornwall) in which brittle fracturing is more common than greisenization, and most mineralization occurs above granite cupolas. Veins commonly exhibit greisenized selvages. Most Cornish tin occurs in steeply dipping lode veins with exploitable strike lengths of hundreds to thousands of meters. The main tin lodes consist of quartz-tourmaline-cassiterite, and are barren of sulfides (Jackson et al., 1989). Homogenization temperatures for these veins range from 275 to 400°C (Jackson et al., 1982; Smith et al., 1996). Stanniferous sulfide-bearing chloritic lodes are less abundant and contain cassiterite-chlorite assemblages with subsequent precipitation of pyrite-chalcopyrite-stannite-sphalerite (Bromley and Holl, 1986) at 200-380°C (Jackson et al., 1982). Mineralization was emplaced at depths of 2-5 km (Smith et al., 1996).
3) Deposits associated with subvolcanic settings (e.g., Bolivia, Cenozoic porphyry samples) and deep subvocanic character (e.g., northern Bolivia, Triassic tin granites), which are dominated by brittle fracture systems above the apical zone of small intrusions. Cassiterite is the most abundant ore mineral of tin, and occurs primarily in quartz, quartz-tourmaline, or quartz-sulfide veins that formed between 510 and 250°C (Sugiyaki and Kitakaze, 1988). Stannite-chalcopyrite-sphalerite-bearing veins postdate main-stage cassiterite mineralization, at 350-230°C (Sillitoe et al., 1975; Sugiyaki and Kitakaze, 1988). Depths of emplacement are estimated to be between 350 and 2000 meters (Kelly and Turneaure, 1970), which implies that the hydrothermal fluids consisted of both liquid and vapor.
4) Pegmatite-hosted disseminated ores of magmatic origin (e.g., Black Hills, South Dakota, USA). Sub-ore grade cassiterite mineralization occurs in the Li-pegmatites of the Keystone region of South Dakota, including the Etta deposit where cassiterite is intergrown with spodumene and feldspar, as well as disseminated within a muscovite-albite matrix (Schwartz, 1925). Stannite also occurs in the Li-pegmatites of the Etta deposit where it is intergrown with chalcopyrite, chalcocite, and bornite (Connolly, 1916). At the nearby Peerless pegmatite, stannite occurs as nodules at the margin of the quartz cores of pegmatite bodies (Černý et al., 2001). The timing relationship between cassiterite and stannite at these localities is uncertain, the importance of these types of deposits is that the

ores formed in a deep setting at ≥8 km depth, as documented by the spodumene-quartz assemblage (London, 1984).

Methodology

Four examples of tin mineralization were selected spanning the four mineralization styles described above, each hosting both cassiterite and stannite: South Dakota, USA (pegmatite), Cornwall, UK (vein-dominated); Cinovec-Krupka camp of the Erzgebirge, Czech Republic (greisen-dominated); Potosi, Bolivia (porphyry). The approach compares minerals from different Sn mineralization styles as a means to identify similar physiochemical reactions across the broad spectrum of tin deposits. The selection of both early cassiterite and late stannite from contrasting settings allows for the evaluation of redox reactions as a potential fractionating mechanism across a range of mineralizing environments.

Due to the fact that the ores are from historic mining districts, all samples are derived from museum collections, and each reported isotope value is from one distinct mineral sample. Samples were obtained from the American Museum of Natural History in New York and the Carnegie Museum of Natural History in Pittsburgh.

Different methods were employed to extract Sn from cassiterite and stannite. Several techniques have been suggested for reduction of Sn from cassiterite (Brügmann et al., 2017; Haustein et al., 2010; Yamazaki et al., 2014) due to its resistance to acid dissolution. In this contribution the methodology of Mathur et al. (2017), a refinement of Haustein et al. (2010), was used: 0.25g of -100 mesh cassiterite powder was mixed with 1 g of KCN and heated at 850°C for one hour in graphite crucibles. The resulting reduced Sn metal beads were dissolved in heated ultrapure 11N HCl overnight. For stannite, 0.05g of powdered sample was dissolved in 15mL teflon jars with ultrapure aqua regia plus trace HF that was heated (100°C) for 12 hours. Complete dissolution was confirmed visually.

For both cassiterite and stannite, a small aliquot was removed and dried for ion exchange chromatography. Solutions were purified using ion exchange chromatography described in Balliana et al. (2013), and employed by Mason et al. (2016) and Mathur et al. (2017). Volumetric yield calculations confirmed the dissolution and recovery of greater than 95% of all Sn from the reduced Sn metal of cassiterite and dissolved stannite samples.

Samples were measured on the Isoprobe at the University of Arizona. Aqueous sample introduction into the plasma was achieved by free aspiration using a microconcentric borosilicate glass nebulizer. Sample uptake rate was approximately 100-150 µL/min. Solutions were kept at 150ppb, which generated a 3-4V signal intensity for ^{120}Sn. The cups were arranged with ^{119}Sn on the axial mass. The remaining mass positions were as follows; ^{116}Sn on low 3, ^{117}Sn on low 2, ^{120}Sn on H1, ^{121}Sb on H2, ^{122}Sn on H3, ^{123}Sb on H4, and ^{124}Sn on H5. The instrument interface was fitted with Ni sample and skimmer cones. The argon gas flow rate of the hexapole collision cell on the Isoprobe was set at 2.5 mL/min. Rinse times between samples was approximately 2-3 minutes. Background intensity for ^{120}Sn ranged from 0.8-1 mV. On-peak blank subtraction was applied to each measurement. Sample measurement consisted of one block of thirty 10 second integration measurements. The intensity of the unknowns matched the signal intensity of the bracketing standard within 20%. Measuring the standard between a 2-5V signal on ^{120}Sn did not produce errors larger than reported.

Mass bias was corrected for by using Sb-doped solutions (High-Purity ICP-MS Sb standard 10 2-3; 10µg/mL in 2% nitric and trace HF) and an exponential mass bias correction defined in Mathur et al. (2017). The corrected values were then bracketed with the NIST 3161A Sn standard. One block of 25 ratios was collected and all samples were measured in duplicate. Data are presented relative to the NIST 3161A Sn standard (Lot# 07033) in per mil notation defined as:

$$\delta^{1xx}\text{Sn‰} = \left(\frac{\left(\frac{\mathbf{1}xx_{Sn}}{\mathbf{116}_{Sn}}\right)sample}{\left(\frac{\mathbf{1}xx_{Sn}}{\mathbf{116}_{Sn}}\right)NIST\ 3161} - \mathbf{1} \right) * 1000$$

Whole procedural 1σ errors for analysis are δ^{120}Sn= 0.04‰ and δ^{124}Sn= 0.08‰ (0.01‰ per amu) for cassiterite as reported in Mathur et al. (2017). This error was calculated by measuring the same sample over 20 times in an effort to refine the reduction procedure and define full procedural errors. Stannite was dissolved and did not experience the KCN reductions. Therefore, the error for stannite measurements is most likely lower. However, the error reported for cassiterite is assumed to be a conservative estimate of errors on stannite Sn

isotope values. To test this, we compared the sample CZR ST 03 measured in two different locations (sample A at the University of Arizona and sample B at Rutgers reported in Table 1). The reported values represent two different powdered portions processed individually from the same stannite mineral separate. Notice that the values fall within the error range described above. Further discussion about the details of analysis and error calculation can be found in Mathur et al. (2017).

Results

The Sn isotope values for a total of 71 samples (50 cassiterite and 21 stannite samples) are reported in Figures 2 and 3, and Table 1. Natural mass dependent fractionation is evident, as the slope of δ^{124}Sn vs. δ^{120}Sn is 2 with an r^2=0.99 (Fig. 2). The two minerals show statistically distinct populations regardless of deposit type, where cassiterite has a higher mean δ^{124}Sn value (+0.48± 0.62‰ (1 σ)) than stannite δ^{124}Sn (-1.47 ± 0.54‰ (1σ)), i.e. a difference of about 2‰.

The reported data are in accord with previous studies. Haustein et al. (2010) report 30 Sn isotope values for Cornish cassiterite. Only one analysis of stannite has been published, with Brügmann et al. (2017) documenting the composition of a sample from Cornwall that was prepared for analysis by co-smelting with copper metal, rather than aqua regia dissolution. Both studies used an in-house standard (Puratronic high-purity foil) for which Brügmann et al. (2017) provide a comparative value for NIST 3161a used herein, allowing for data conversion. The converted mean δSn of 0.11 ± 0.08‰ per amu for cassiterite from Cornwall reported by Haustein et al. (2010) is statistically equivalent to the findings of this study (0.12 ± 0.03‰ per amu; n=11). Furthermore, both Brügmann et al. (2017) and this study found a distinctly lower value of δSn for Cornish stannite relative to NIST 3161a, -0.06 ± 0.05‰ per amu (n=1) and -0.19 ± 0.04‰ per amu (n=5), respectively. This reproducibility demonstrates that differing preparation methods yield consistent analytical results for both cassiterite and stannite. No published data sets of Sn isotope compositions exist for minerals from Bolivia or South Dakota.

The mean values of cassiterite and stannite show similar variation across the four deposits studied, with a δ^{124}Sn range of 2.48‰ for cassiterite and 2.61‰ for stannite. However, in each of the four deposits studied, Sn in stannite has lower values than cassiterite.

To quantify this relationship, a comparison of the mean values of the two phases within different deposits was calculated using the following expression:

$$\Delta^{124}Sn_{cassiterite-stannite} = \text{mean } \delta^{124}Sn_{cassiterite} - \text{mean } \delta^{124}Sn_{stannite}$$

Tin mineralization from all four ore districts has similar values: 2.3‰± 0.2 ‰ (Cornwall), 2.1‰ ± 0.2 ‰ (South Dakota), 2.0‰ ± 0.2 ‰ (Cinovec-Krupka), and 1.5‰ ± 0.2 ‰ (Bolivia) (Fig. 2). Thus, each locality displays a similar and consistent shift in Sn isotopic composition between cassiterite and stannite regardless of mineralization style and depth of emplacement. However, the shallowest deposits are associated with the lowest $\Delta^{124}Sn_{cassiterite-stannite}$ values.

Insights into Causes of Sn isotope Fractionation in Ores

Fractionation of Sn isotopes in hydrothermal mineralizing systems may be related to multiple inter-related variables: speciation of Sn into different compounds in solution, liquid-vapor partitioning, electron transfer, temperature, pressure, the competitive bonding environment, and equilibrium processes associated with partitioning of Sn into different phases. There is a dearth of experimental studies that isolate these factors associated with ore deposit genesis. However, empirical evidence derived from ore minerals associated with known geochemical reactions and processes have been used commonly as a means to constrain the causes for isotopic fractionation in mineralizing systems using other metal isotope systems: Fe (Bilenker et al., 2016; Zhu et al., 2018) , Ni (Liu et al., 2018), Cu (Maher et al., 2011; Markl et al., 2006; Mathur et al., 2013), Zn (Gagnevin et al., 2012; Zhou et al., 2014), Mo ((Greber et al., 2011; Yao et al., 2016), Ag (Mathur et al., 2018) and Te (Fornadel et al., 2014).

Given the geological context of the samples, several of the above mechanisms can be eliminated. The consistent variation of Sn isotope values between cassiterite and stannite presented here persists for deposits that formed in deep vapor-absent environments (pegmatites of South Dakota) up to the subvolcanic settings (porphyries in Bolivia), indicating that pressure changes, temperature variations, and liquid-vapor transitions cannot be the causative mechanism for the observed fractionation. The similarities in mineralogical paragenesis in these systems (where cassiterite in these systems clearly predates stannite and no cogenetic sulfides exist with cassiterite) excludes equilibrium partitioning among phases or

within-solution speciation as a clear-cut mechanism. As demonstrated by Eugster (1985), Sn in hydrothermal tin systems is in the form of chloride complexes. SnO_2 has a broad stability field at high T, while with decreasing temperature the stannite field expands.

Differing bond energies associated with precipitation of Sn with O and S could be related to fractionation. The bond distance difference between the two ligands is 0.25 picometers (Smith, 2012). Theoretical fractionation factors can be calculated using these bond lengths (as has been done with other metal isotopes, Seo et al., 2007), however as pointed out with Fe isotope fractionation factors determined by (Sossi and O'Neill, 2017) a significant discrepancy exists between theoretical and experimental determined fractionation factors. Nevertheless, the potential exists that within solution speciation may affect fractionation when Sn-O and Sn-Cl species exist during precipitation of cassiterite. Germane to this argument, given the mass balance that must occur in the system and no sulfides form paragenetically early in these systems, the initial redox of Sn from the hydrothermal solution is the most likely mechanism for fractionation.

It is well-established that tin is transported in hydrothermal fluids in the reduced state (Sn^{2+}), and that formation of cassiterite and stannite requires an oxidative transition to Sn^{4+}. Furthermore, it has been demonstrated repeatedly that oxidation of multi-valent metals imparts significant isotopic fractionation favoring the heavy isotope (Dauphas et al., 2009; Dauphas et al., 2014; Domagal-Goldman and Kubicki, 2008; Sherman, 2013). For some metals, such as Cu, oxidation-induced fractionation is observed in the products of low-temperature, near-surface reactions (Mathur et al., 2010). In cases such as Fe, identifying the component of fractionation associated with redox reactions is confounded by overprints due to numerous coincident fractionation mechanisms, particularly partitioning between coexisting phases (Dauphas et al., 2014). Neither weathering, nor partitioning between co-existing phases, complicate the Sn system in the hydrothermal setting examined in this study.

Based on inelastic nuclear resonant X-ray scattering (INRXS) and Mössbauer spectroscopy experiments, Polyakov et al. (2005) predicted that oxidation state would have a large effect on fractionation of Sn. Since neither low-temperature processes nor partitioning between co-precipitating minerals complicate the hydrothermal Sn isotopic system examined here, fractionation due to high-temperature redox changes likely would be evident. In each of

the four tin camps studied there is a large Sn isotopic variation between early cassiterite and later stannite, between 1.5 and 2.4‰ in δ^{124}Sn. Given the oxidation-dependent mechanism for cassiterite precipitation (Heinrich, 1990), and the results of the synchrotron experiments of Polyakov et al. (2005), this isotopic shift is most likely attributable to the oxidation of Sn^{2+} in the hydrothermal fluids. Oxidation-driven precipitation of cassiterite left the hydrothermal solution enriched in tin of lighter isotopic composition. Subsequent oxidation of the residual Sn^{2+} resulted in the precipitation of stannite with negative δ^{124}Sn values, inheriting the residual Sn isotope composition of the fluid. It is also possible that within solution speciation of Sn-S and Sn-O bonds could impart some degree of fractionation.

The fractionation factor and relative mass of Sn residing in different reservoirs can be approximated and used to model Sn isotope values in cassiterite and stannite. Creech et al. (2017) provide a Sn isotopic composition of the USGS standard GSP-2 (δ^{122}Sn= +0.19‰, where δ^{122}Sn is ^{122}Sn/^{118}Sn and is equivalent to δ^{120}Sn presented here), a granodiorite from the ca. 1400 Ma metaluminous to peraluminous Silver Plume granitoid suite, Colorado (Bender, 1983). This is the only granitic Sn isotope composition reported in the literature. Although the standards used to bracket the data in Creech et al. (2017) and here are different, Brügmann et al. (2017) point out that several ICP-MS standards are within 0.1 per mil of the 3160 NIST standard reported here, and thus adequate to construct a first order geochemical model. A Proterozoic lower crust is the likely source for the generation of the Erzgebirge tin-granites (Bankwitz and Bankwitz, 1994). Accordingly, GSP-2 is adopted as a reasonable starting composition for the tin composition of magmas (δ^{124}Sn= +0.40‰) associated with the Erzgebirge, which corresponds to a fractionation factor between the starting fluid and average cassiterite of $\alpha_{solution\text{-}solid}$=1.0003. Rayleigh distillation equations presented in Faure (1986) yield results where the first 80% (Fig. 4) of the Sn precipitated from the hydrothermal fluid would have δ^{124}Sn values between 0.2 to +0.6 ‰ which is congruent with the distribution of Sn isotope values for Cornwall, Erzgebirge and Bolivia in Table 1.

The model also demonstrates that in order to obtain solutions and solids corresponding to the stannite values, greater than 99.5% all of Sn in the system must have precipitated in the form of cassiterite. This is consistent with the relative abundance of these two minerals in tin ores globally; although stannite is widely distributed in sulfide ores associated with tin

mineralization, it is a very minor component and rarely of economic interest. Even if the fractionation factor is doubled, the model still predicts the Sn isotope values documented in cassiterite and stannite. The mass balance of the solutions in this model dictates that the remaining solutions must possess a significantly larger proportion of lighter Sn when the stannite is formed in the system.

While it is possible that Sn-S bonding from solution to solid would induce the fractionation seen, the mass balance of Sn in the system predicts that the remaining solution must possess proportionately significant lighter Sn. Therefore, the simple distillation model predicts the range of Sn isotope values observed in both phases using a fractionation factor most likely triggered by electron transfer in the hydrothermal solution. Further higher temperature experimentation will elucidate if redox is the sole mechanism or different bonding energies associated with the formation of Sn-S to form stannite control fractionation.

Although oxidation-related isotopic fractionation is evident in the four localities regardless of mineralization style, there is a range of the $\Delta^{124}Sn_{cassiterite\ -\ stannite}$ values. This variation could be due to variations in the efficiency of cassiterite precipitation; lower yields of early cassiterite would result in lower values of $\Delta^{124}Sn_{cassiterite-stannite}$. Alternatively, this range could be related to additional fractionation mechanisms. Partitioning of Sn between brine and vapor in a shallow setting likely induces fractionation, similar to that observed in the distillation experiments of Mathur et al. (2017). Fractionation due to partitioning of Sn between vapor and fluid at shallow depths could impart a shift in the isotopic composition of the fluids from which stannite precipitates. This would be consistent with the observed variation in $\Delta^{124}Sn_{cassiterite-stannite}$ values and standard deviation of $\delta^{124}Sn$ of cassiterite from the hydrothermal ores: highest $\Delta^{124}Sn_{cassiterite\ -\ stannite}$ (2.3) and lowest standard deviation (± 0.21‰) at Cornwall with the greatest emplacement depth (5-6 km; Pownall et al., 2012; Drivens et al. 2016), lower (2.0 ± 0.46) at Cinovec (Zinnwald) at intermediate depth (1-2 km; Korges et al., 2018), and lowest $\delta^{124}Sn_{cassiterite-stannite}$ (1.5) for the shallowest deposits in Bolivia (<1.5 km; Sillitoe et al. 1975) (Fig. 3).

Implications and Future Directions for Sn Isotopic Analysis

399 The current study demonstrates that oxidation of Sn at high temperature causes
400 predictable fractionation of Sn isotopes. Fractionation of the Sn isotope system may provide a
401 better monitor of high-temperature redox reactions than those in which such signatures may
402 be masked by isotopic partitioning between coexisting phases (e.g., Fe). Furthermore, the
403 stability of cassiterite in the surface environment preserves its isotopic signature throughout
404 the weathering process. Accordingly, Sn isotopes have great potential as a broadly applicable
405 analytical tool. They may be used to identify source rocks and monitor redox changes in
406 magmatic-hydrothermal systems, even in highly weathered settings. Sn isotopic analysis can
407 also provide insights into the processes associated with rare-element granite mineralization. In
408 addition, Sn isotope analysis is a powerful tool for provenance studies of bronze artifacts,
409 allowing archaeologists to match artifacts to a known tin source, or to refine their search
410 parameters for a specific tin source by inferring deposit characteristics from the Sn isotope
411 signatures of bronze artifacts.

412

413 **Acknowledgements:**

414 This work is supported by the National Key R&D Program of China (2016YFC0600405), the
415 National Natural Science Foundation of China (Nos. 41672079, 41372085) and Strategic Priority
416 Research Program (B) of the Chinese Academy of Sciences (XDB1803206).

417

418 **References**

419 Badullovich, N., Moynier, F., Creech. J., Teng, F., and Sossi, P. (2107) Tin isotopic fractionation
420 during igneous differentiation and Earth's mantle deposition. Geochemical Perspectives
421 Letters, 5, 24-28.
422 Balliana, E., Aramendía, M., Resano, M., Barbante, C., Vanhaecke, F. (2013) Copper and tin
423 isotopic analysis of ancient bronzes for archaeological investigation: development and
424 validation of a suitable analytical methodology. Analytical and Bioanalytical Chemistry,
425 405, 2973-2986.
426 Bankwitz, P., and Bankwitz, E. (1994) Crustal structure of the Erzgebirge: Metallogeny of
427 Collisional Orogens. Czech Geological Survey, Prague, p. 20-34.
428 Bender, R.B. (1983), Petrology and geochemistry of the Silver Plume-age plutons of the
429 southern and central Wet Mountains, Colorado. Unpublished PhD Thesis, Louisiana
430 State University, Baton Rouge, 200p.
431 Bilenker, L. D., Simon, A. C., Reich, M., Lundstrom, C. C., Gajos, N., Bindeman, I., Barra, F., and
432 Munizaga, R. (2016) Fe–O stable isotope pairs elucidate a high-temperature origin of
433 Chilean iron oxide-apatite deposits: Geochimica et Cosmochimica Acta, v. 177, p. 94-
434 104.Borrok, D., Nimick, D., Wanty, R., Ridley, W., 2008, Isotopic variations of dissolved
435 copper and zinc in stream waters affected by historical mining. Geochimica et
436 Cosmochimica Acta, 72, 329-344.
437 Borrok, D., Nimick, D., Wanty, R., Ridley, W. (2008) Isotopic variations of dissolved copper and
438 zinc in stream waters affected by historical mining. Geochimica et Cosmochimica Acta,
439 72, 329-344.
440 Bromley, A., and Holl, C. (1986) Tin mineralization in Southwest England, in Wills, B., and Barley,
441 R. (eds.) Mineral Processing at a Crossroads. Dordrecht, Matrinus Nijhoff, p. 195-262.
442 Bankwitz, P., and Bankwitz, E. (1994) Crustal structure of the Erzgebirge. Metallogeny of
443 Collisional Orogens. Czech Geological Survey, Prague, p. 20-34.
444 Brügmann, G., Berger, D., and Pernicka, E. (2017) Determination of the tin stable isotopic
445 composition in tin-bearing metals and minerals by MC-ICP-MS. Geostandards and
446 Geoanalytical Research, 41, 437-448
447 Brugger, J., Liu, W., Etschmann, B., Mei, Y., Sherman, D.M., Testemale, D. (2016) A review of the
448 coordination chemistry of hydrothermal systems, or do coordination changes make ore
449 deposits? Chemical Geology, 447, 219-253.
450 Campbell, A., and Panter, K. (1990) Comparison of fluid inclusions in coexisting (cogenetic?)
451 wolframite, cassiterite,and quartz from St. Michael's Mount and Cligga Head, Cornwall,
452 England. Geochimica et Cosmochimica Acta, 54, 673-681.
453 Černý, P., Masau, M., Ercit, T.S., Chapman, R., and Chackowsky, L. (2001) Stannite and kesterite
454 from the Peerless pegmatite, Black Hills, South Dakota, USA. Journal of the Czech
455 Geological Society, 46, 27-33.
456 Černý, P., Blevin, P., Cuney, M., and London, D. (2005) Granite-related ore deposits, in
457 Heldenquist, J., Thompson, J., Goldfarb, R., and Richards, J., eds., Economic Geology One
458 Hundredth Anniversary Volume 1905-2005, Society of Economic Geologists, p. 337-370.
459 Chen, X.C., Hu, R.Z., Bi, X.W., Li., H.M., Lan, J.B., Zhao, C.H., and Zhu, J.J. (2014) Cassiterite LA-
460 MC-ICP-MS U/Pb and muscovite 40Ar/39Ar dating of tin deposits in the Tengchong-
461 Lianghe tin district, NW Yunnan, China. Mineralium Deposita, 49, 843-860.

462 Chicharro, E., Boiron, M.C., Lopez-Garcia, J., Barfod, D., and Villaseca, C. (2016) Origin, ore
463 forming fluid evolution and timing of the Logrosán Sn-(W) ore deposits (Central Iberian
464 Zone, Spain). Ore Geology Reviews, 72, 896-913.
465 Connolly, J. (1916) Rare minerals in the Black Hills as state assets. Proceedings of the South
466 Dakota Academy of Science Proceedings, 1, 40-53.
467 Creech, J. B., Moynier, F., and Badullovich, N. (2017) Tin stable isotope analysis of geological
468 materials by double-spike MC-ICPMS. Chemical Geology, 457, 61-67.
469 Dauphas, N., Craddock, P. R., Asimow, P. D., Bennett, V. C., Nutman, A. P., and Ohnenstetter, D.
470 (2009) Iron isotopes may reveal the redox conditions of mantle melting from Archean to
471 Present. Earth and Planetary Science Letters, 288, 255-267.
472 Dauphas, N., Roskosz, M., Alp, E., Neuville, D., Hu, M., Sio, C., Tissot, F., Zhao, J., Tissandier, L.,
473 and Médard, E. (2014) Magma redox and structural controls on iron isotope variations in
474 Earth's mantle and crust. Earth and Planetary Science Letters, 398, 127-140.
475 Domagal-Goldman, S. D., and Kubicki, J. D. (2008) Density functional theory predictions of
476 equilibrium isotope fractionation of iron due to redox changes and organic
477 complexation. Geochimica et Cosmochimica Acta, 72, 5201-5216.
478 Drivenes, K., Larsen, R., Müller, A., and Sørensen, B. (2016) Crystallization and uplift path of late
479 Variscan granites evidenced by quartz chemistry and fluid inclusions: Example from the
480 Land's End granite, SW England. Lithos, 252-253, 57-75.
481 Eibschütz, M., Hermon, E., and Shtrikman, S. (1967) Determination of cation valencies in
482 $Cu_2{}^{57}Fe^{119}SnS_4$ by Mössbauer effect and magnetic susceptibility measurements. Journal
483 of Physics and Chemistry of Solids, 28, 1633–1636.
484 Eugster, H., and Wilson, G. (1985) Transport and deposition of ore-forming elements in
485 hydrothermal systems associated with granites, in Halls, C., ed., High heat production
486 (HPP) granites, hydrothermal circulation and ore genesis. Institution of Mining and
487 Metallurgy, p. 87-98.
488 Farges, F., Linnen, R., and Brown, G. Jr. (2006) Redox and speciation of tin in hydrous silicate
489 glasses: A comparison with Nb, Ta, Mo and W. The Canadian Mineralogist, 44, 795-810.
490 Faure, G. (1986) Principles of isotope geology. New York, NY, John Wiley & Sons,.
491 Fornadel, A. P., Spry, P. G., Jackson, S. E., Mathur, R. D., Chapman, J. B., and Girard, I. (2014)
492 Methods for the determination of stable Te isotopes of minerals in the system Au-Ag-Te
493 by MC-ICP-MS. Journal of Analytical Atomic Spectrometry, 29, 623-637.
494 Gagnevin, D., Boyce, A. J., Barrie, C. D., Menuge, J. F., and Blakeman, R. J. (2012) Zn, Fe and S
495 isotope fractionation in a large hydrothermal system. Geochimica et Cosmochimica
496 Acta, 88, 183-198.
497 Greber, N. D., Hofmann, B. A., Voegelin, A. R., Villa, I. M., and Nägler, T. F. (2011) Mo isotope
498 composition in Mo-rich high- and low-T hydrothermal systems from the Swiss Alps.
499 Geochimica et Cosmochimica Acta, 75, 6600-6609.
500 Greenwood, N., and Whitfield, H. (1968) Mössbauer effect studies on cubanite ($CuFe_2S_3$) and
501 related iron sulphides. Journal of the Chemical Society A Inorganic Physical Theoretical,
502 7, 1697-1699.
503 Haustein, M., Gillis, C., and Pernicka, E. (2010) Tin isotopy—a new method for solving old
504 questions. Archaeometry, 52, 816-832.

505 Heinrich, C. (1990) The chemistry of hydrothermal tin(-tungsten) ore deposition. Economic
506 Geology, 85, 457-481.
507 Heinrich, C., and Ryan, C. (1992) Mineral paragenesis and regional zonation of granite-related
508 Sn-As-Cu-Pb-Zn deposits: A chemical model for the Mole Granite district (Australia)
509 based on PIXE fluid inclusion analyses, in: Kharaka, Y., and Maest, A (eds.),Water-Rock
510 Interaction, Proceedings on the 7th International Symposium on Water-Rock
511 Interaction, p. 1583-1587.
512 Imeokparia, E. (1982) Tin content of biotites from the Afu younger granite complex, Central
513 Nigeria. Economic Geology, 77, 1710-1724.
514 Jackson, N., Halliday, A., Sheppard, S., and Mitchell, J. (1982) Hydrothermal activity in the St.
515 Just mining district, Cornwall, England, in Evans A. (ed.) Metallization Associated with
516 Acid Magmatistm. Chichester, Wiley, p. 137-179.
517 Jackson, N., Willis-Richards, J., Manning, D., and Sams, M. (1989) Evolution of the Cornubian
518 Ore Field, Southwest England: Part II. Mineral deposits and ore-forming processes.
519 Economic Geology, 84, 1101-1133.
520 Kelly, W., and Turneaure, F. (1970) Mineralogy, paragenesis and geothermometry of the tin and
521 tungsten deposits of the Eastern Andes, Bolivia. Economic Geology, 65, 609-680.
522 Korges, M., Weis, P., Lüders, V., and Laurent, O. (2018) Depressurization and boiling of a single
523 magmatic fluid as a mechanism for tin-tungsten deposit formation. Geology, 46, 75-78.
524 Lehmann, B. (1982) Metallogeny of tin: Magmatic differentiation versus geochemical heritage.
525 Economic Geology, 77, 50-59.
526 Lehmann, B. (1987) Tin granites, geochemical heritage, magmatic differentiation. Geologische
527 Rundschau, 76, 177-185.
528 Linnen, R., Pichavant, M., Holtz, F., and Burgess, S. (1995) The effect of fO_2 on the solubility,
529 diffusion, and speciation of tin in haplogranitic melt at 850°C and 2 kbar. Geochimica et
530 Cosmochimica Acta, 59, 1579-1588.
531 Linnen, R., Pichavant, M., and Holtz, F. (1996) The combined effects of fO_2 and melt
532 composition on SnO_2 solubility and tin diffusivity in haplogranitic melts. Geochimica et
533 Cosmochimica Acta, 60, 4965-4976.
534 Liu, S., Li, Y., Ju, Y., Liu, J., Liu, J., and Shi, Y. (2018) Equilibrium nickel isotope fractionation in
535 nickel sulfide minerals. Geochimica et Cosmochimica Acta, 222, 1-16.
536 London, D. (1984) Experimental phase equilibria in the system $LiAlSiO_4$-SiO_2-H_2O: a petrogenetic
537 grid for lithium-rich pegmatites. American Mineralogist, 69, 995-1004.
538 Maher, K. C., Jackson, S., and Mountain, B. (2011) Experimental evaluation of the fluid–mineral
539 fractionation of Cu isotopes at 250°C and 300°C. Chemical Geology, 286, 229-239.
540 Markl, G., and Schumacher, J. (1996) Spatial variations in temperature and composition of
541 greisen-forming fluids: An example from the Variscan Triberg Granite Complex,
542 Germany. Economic Geology, 91, 576-589.
543 Markl, G., Lahaye, Y., and Schwinn, G. (2006) Copper isotopes as monitors of redox processes in
544 hydrothermal mineralization. Geochimica et Cosmochimica Acta, 70, 4215-4228.
545 Mason, A., Powell, W., Bankoff, H., Mathur, R., Bulatović, A., Filipović, V., and Ruiz, J. (2016) Tin
546 isotope characterization of bronze artifacts of the central Balkans. Journal of
547 Archaeological Science, 69, 110-117.

548 Mathur, R., Arribas, A., Megaw, P., Wilson, M., Stroup, S., Meyer-Arrivillaga, D., and Arribas, I.
549 (2018) Fractionation of silver isotopes in native silver explained by redox reactions.
550 Geochimica et Cosmochimica Acta, 224, 313-326.
551 Mathur, R., Munk, L., Nguyen, M., Gregory, M., Annell, H., and Lang, J. (2013) Modern and
552 paleofluid pathways revealed by Cu isotope compositions in surface waters and ores of
553 the Pebble porphyry Cu-Au-Mo deposit, Alaska. Economic Geology, 108, 529-541.
554 Mathur, R., Dendas, M., Titley, S., Phillips, A. (2010) Patterns in the copper isotopic composition
555 of minerals in porphyry copper deposits in the Southwestern United States of America.
556 Economic Geology, 105, 1457-1467.
557 Mathur, R., Powell, W., Mason, A., Godfrey, L., Yao, J., and Baker, M. E. (2017) Preparation and
558 measurement of cassiterite for Sn isotope analysis. Geostandards and Geoanalytical
559 Research, 41, 701-707.
560 Neiva, A. (1976) The geochemistry of biotites from granites of northern Portugal with special
561 reference to their tin content. Mineralogical Magazine, 40, 453-466.
562 Plimer, I. (1984) Mayayaite and tin-bearing silicates from a skarn at Doradilla via Bourke, New
563 South Wales. Australian Journal of Earth Sciences, 31, 147-153.
564 Plimer, I. (1987) Fundamental parameters for the formation of granite-related tin deposits.
565 Geologische Rundschau, 76, 23-40.
566 Pokrovsky, O., Viers, J., Emnova, E., Kompantseva, E., Freydier, R. (2008) Copper isotope
567 fractionation during its interaction with soil and aquatic microorganisms and metal
568 oxy(hydr)oxides; possible structural control. Geochimica et Cosmochimica Acta, 72,
569 1742-1757.
570 Polyakov, V., Mineev, S., Clayton, R., Hu, G., and Mineev, K. (2005) Determination of equilibrium
571 isotope fractionation factors from synchotron radiation experiments. Geochimica et
572 Cosmochimica Acta, 69, 5531-5536.
573 Pownall, J., Waters, D., Searle, M., Shail, R., and Robb, L. (2012) Shallow laccolithic
574 emplacement of the Land's End and Tregonning granites, Cornwall, UK: Evidence from
575 aureole field relations and P-T modeling of cordierite-anthophyllite hornfels. Geosphere,
576 8, 1467-1504.
577 Radivojević, M., Rehren, T., Kuzmanović-Cvetković, J., Jovanović, M., Northover, J. (2013)
578 Tainted ores and the rise of tin bronze metallurgy, c. 6500 years ago, Antiquity, 87,
579 1030-1045.
580 Rudnick, R., and Gao, S. (2003) Composition of the continental crust. Treatise on Geochemistry,
581 3, 1-64.
582 Schwartz, G. (1925) Geology of the Etta spodumene mine, Black Hills, South Dakota. Economic
583 Geology, 20, 646-659.
584 Sherman, D. M. (2013) Equilibrium isotopic fractionation of copper during oxidation/reduction,
585 aqueous complexation and ore-forming processes: Predictions from hybrid density
586 functional theory. Geochimica et Cosmochimica Acta, 118, 85-97.
587 Sillitoe, R., Halls, C., and Grant, J. (1975) Porphyry tin deposits in Bolivia. Economic Geology, 70,
588 913-927.
589 Smith, P. J. (2012) Chemistry of Tin. Springer, 578 p.

Smith, M., Banks. D., Yardley, B., and Boyce, A. (1996) Fluid inclusion and stable isotope constraints on the genesis of the Cligga Head Sn-W deposit, S.W. England. European Journal of Mineralogy, 8, 961-974.

Sossi, P. A., and O'Neill, H. S. C. (2017) The effect of bonding environment on iron isotope fractionation between minerals at high temperature. Geochimica et Cosmochimica Acta, 196, 121-143.

Sugaki, A., Ueno, H., Shimada, M., Kitakaze, A., Shima, H., Sansines, O., and Saavedra, A. (1981) Geological study on polymetallic hydrothermal deposits in the Oruro District, Bolivia. Science Reports, Tohoku University, Series 3: Mineralogy, Petrology, and Economic Geology, 15, 1-52.

Taylor, R. (1979) The geology of tin deposits; Developments in Economic Geology v. 11, Elsevier, 543 p.

Wang, R., Xie, L., Chen, J., Yu, A, Wang, L., Lu, J., and Zhu, J. (2013) Tin-carrier minerals in metaluminous granites of the western Nanling Range (southern China): Constraints on processes of tin mineralization in oxidized granites. Journal of Asian Earth Sciences, 74, 361-372.

Yamazaki, E., Nakai, S., Sahoo, Y., Yokoyama, T., Mifune, H., Saito, T., Chen, J., Takagi, N., Hokanishi, N., and Yasuda, A. (2014) Feasibility studies of Sn isotope composition for provenancing ancient bronzes. Journal of Archaeological Science, 52, 458-467.

Yao, J., Mathur, R., Sun, W., Song, W., Chen, H., Mutti, L., Xiang, X., and Luo, X. (2016) Fractionation of Cu and Mo isotopes caused by vapor-liquid partitioning, evidence from the Dahutang W-Cu-Mo ore field. Geochemistry, Geophysics, Geosystems, 17, 1725-1739.

Yuan, S., Peng, J., Hao, S., Li, H., Geng, J., and Zhang, D. (2011) In situ LA-MC-ICP-MS and ID-TIMS U–Pb geochronology of cassiterite in the giant Furong tin deposit, Hunan Province, South China: New constraints on the timing of tin–polymetallic mineralization. Ore Geology Reviews, 43, 235-242.

Zhang, R., Lu, J., Wang, R., Yang, P., Zhu, J., Yao, Y., Gao, J., Li, C., Lei, Z., Zhang, W., and Guo, W. (2015) Constraints of in situ zircon and cassiterite U–Pb, molybdenite Re–Os and muscovite ^{40}Ar–^{39}Ar ages on multiple generations of granitic magmatism and related W–Sn mineralization in theWangxianling area, Nanling Range, South China. Ore Geology Reviews, 65, 1023-1042.

Zhang, R., Lehmann, B., Seltmann, R., Sun, W., Li, C. (2017) Cassiterite U-Pb geochronology constrains magmatic-hydrothermal evolution in complex evolved granite systems: The classic Erzgebirge tin province (Saxony and Bohemia). Geology, 45, 1095-1098.

Zhou, J.-X., Huang, Z.-L., Zhou, M.-F., Zhu, X.-K., and Muchez, P. (2014) Zinc, sulfur and lead isotopic variations in carbonate-hosted Pb–Zn sulfide deposits, southwest China. Ore Geology Reviews, 58, 41-54.

Zhu, Z.-Y., Jiang, S.-Y., Mathur, R., Cook, N. J., Yang, T., Wang, M., Ma, L., and Ciobanu, C. L. (2018) Iron isotope behavior during fluid/rock interaction in K-feldspar alteration zone – A model for pyrite in gold deposits from the Jiaodong Peninsula, East China: Geochimica et Cosmochimica Acta, 222, Supplement C, 94-116.

Figure Captions:

Figure 1- Cartoon cross section depicting key differences in the deposit types analyzed along with Sn isotope difference between cassiterite and stannite for deposits analyzed. Oxidation reactions at high temperatures induce distinct isotopic signatures. The example from South Dakota would be a signifcantly greater depth with pegamtitic fluids being the source of mineralization.

Figure 2- Mass dependence of cassiterite and stannite data, the slope of the presented line =2. The relative clustering of the different minerals is evident.

Figure 3- Tin isotope ranges of the minerals for each deposit. Grey bars indicate range of cassiterite and stannite values for each deposit.

Figure 4- Rayliegh distillation model which predicts the range of fluids that would evolve from a granitic magma where f is a proportion of Sn in magma/ Sn in fluid . The grey box highlights the range of Sn isotope values for cassiterite assuming fractionation occurred during redox reactions that led to the precipitation of cassiterites. The model predicts the largest Sn isotope value precipitated earliest.

Table 1- Deposit location, phase and Sn isotope data for each sample.

Study #	Country	Region	Mineral	δ^{120}Sn ‰	δ^{124}Sn ‰
BOL 06	Bolivia	Oruro	Cassiterite	0.06	0.08
BOL 07	Bolivia	Potosi	Cassiterite	-0.32	-0.60
BOL 08	Bolivia	Potosi	Cassiterite	0.39	0.70
BOL 09	Bolivia	Potosi	Cassiterite	0.38	0.71
BOL 10	Bolivia	Potosi	Cassiterite	0.20	0.33
BOL 11	Bolivia	Potosi	Cassiterite	0.40	0.80
BOL 12	Bolivia	Potosi	Cassiterite	0.48	0.89
BOL 13	Bolivia	Potosi	Cassiterite	0.31	0.58
BOL 14	Bolivia	Potosi	Cassiterite	0.21	0.40
CZR 01	Czech Republic	Erzgebirge	Cassiterite	0.43	0.81
CZR 02	Czech Republic	Erzgebirge	Cassiterite	0.26	0.48
CZR 03	Czech Republic	Erzgebirge	Cassiterite	0.02	0.11
CZR 04	Czech Republic	Erzgebirge	Cassiterite	0.07	0.20
CZR 05	Czech Republic	Erzgebirge	Cassiterite	0.51	0.97
CZR 06	Czech Republic	Erzgebirge	Cassiterite	0.60	1.12
CZR 07	Czech Republic	Erzgebirge	Cassiterite	0.57	1.11
CZR 08	Czech Republic	Erzgebirge	Cassiterite	0.58	1.07
CZR 09	Czech Republic	Erzgebirge	Cassiterite	0.03	0.01
CZR 10	Czech Republic	Erzgebirge	Cassiterite	0.48	0.90
CZR 11	Czech Republic	Erzgebirge	Cassiterite	0.58	1.08
CZR 12	Czech Republic	Erzgebirge	Cassiterite	0.56	1.02
CZR 13	Czech Republic	Erzgebirge	Cassiterite	-0.02	-0.12
CZR 14	Czech Republic	Erzgebirge	Cassiterite	0.69	1.23
CZR 15	Czech Republic	Erzgebirge	Cassiterite	0.28	0.50
CZR 16	Czech Republic	Erzgebirge	Cassiterite	0.39	0.90
CZR 17	Czech Republic	Erzgebirge	Cassiterite	0.39	0.75
CZR 18	Czech Republic	Erzgebirge	Cassiterite	0.46	0.77
CZR 19	Czech Republic	Erzgebirge	Cassiterite	0.51	0.91
CZR 20	Czech Republic	Erzgebirge	Cassiterite	-0.17	-0.37
CZR 21	Czech Republic	Erzgebirge	Cassiterite	0.70	1.27
CZR 22	Czech Republic	Erzgebirge	Cassiterite	0.26	0.44
ENG 01	England	Cornwall	Cassiterite	0.52	1.09
ENG 02	England	Cornwall	Cassiterite	0.67	1.20
ENG 03	England	Cornwall	Cassiterite	0.39	0.75
ENG 04	England	Cornwall	Cassiterite	0.28	0.68
ENG 08	England	Cornwall	Cassiterite	0.57	1.13
ENG 09	England	Cornwall	Cassiterite	0.42	0.82
ENG 10	England	Cornwall	Cassiterite	0.25	0.54

ENG 11	England	Cornwall	Cassiterite	0.30	0.56
ENG 13	England	Cornwall	Cassiterite	0.43	0.80
ENG 14	England	Cornwall	Cassiterite	0.44	0.81
ENG 15	England	Cornwall	Cassiterite	0.47	0.87
USA 01	USA	South Dakota	Cassiterite	-0.60	-1.18
USA 02	USA	South Dakota	Cassiterite	0.04	0.12
USA 03	USA	South Dakota	Cassiterite	-0.61	-1.14
USA 04	USA	South Dakota	Cassiterite	-0.19	-0.32
USA 05	USA	South Dakota	Cassiterite	-0.02	-0.02
USA 06	USA	South Dakota	Cassiterite	-0.04	-0.09
USA 07	USA	South Dakota	Cassiterite	-0.57	-1.10
USA 08	USA	South Dakota	Cassiterite	-0.32	-0.57
CZR ST 03a	Czech Reb	Erzgebirge	Stannite	-0.65	-1.18
CZR ST 03b	Czech Reb	Erzgebirge	Stannite	-0.60	-1.25
BOL 15	Bolivia	Potosi	Stannite	-0.91	-1.84
BOL 16	Bolivia	Potosi	Stannite	0.00	-0.27
BOL 18	Bolivia	Oruro	Stannite	-0.86	-1.83
BOL 19	Bolivia	Oruro	Stannite	-0.55	-1.12
BOL 20	Bolivia	Oruro	Stannite	-0.59	-0.88
BOL 21	Bolivia	Potosi	Stannite	-0.51	-0.87
CZR 23	Czech Reb	Erzgebirge	Stannite	-0.98	-1.56
CZR 24	Czech Reb	Erzgebirge	Stannite	-0.51	-1.13
ENG 16	England	Cornwall	Stannite	-0.81	-1.46
ENG 17	England	Cornwall	Stannite	-0.62	-1.15
ENG 18	England	Cornwall	Stannite	-0.57	-1.38
ENG 19	England	Cornwall	Stannite	-0.89	-1.59
ENG 20	England	Cornwall	Stannite	-0.94	-1.87
ENG 21	England	Cornwall	Stannite	-0.81	-1.46
ENG 22	England	Cornwall	Stannite	-0.62	-1.15
ENG 23	England	Cornwall	Stannite	-0.57	-1.38
ENG 24	England	Cornwall	Stannite	-0.89	-1.59
ENG 25	England	Cornwall	Stannite	-0.94	-1.87
USA 09	USA	South Dakota	Stannite	-1.12	-2.41
USA 10	USA	South Dakota	Stannite	-1.71	-2.88

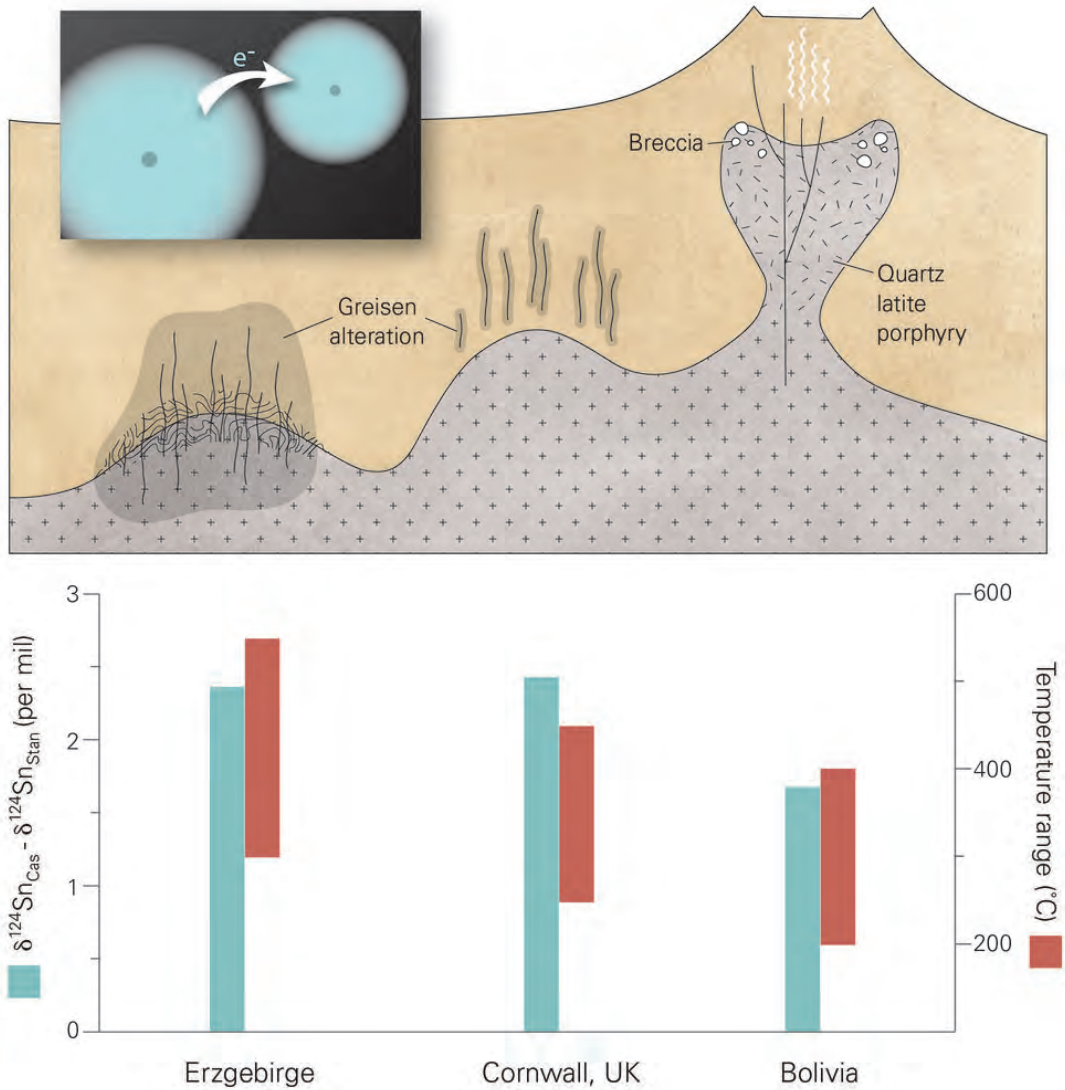
e⁻
Breccia
Quartz
latite
porphyry
Greisen
alteration
3
2
1
0
600
400
200
δ124SnCas - δ124SnStan (per mil)
Temperature range (°C)
Erzgebirge
Cornwall, UK
Bolivia

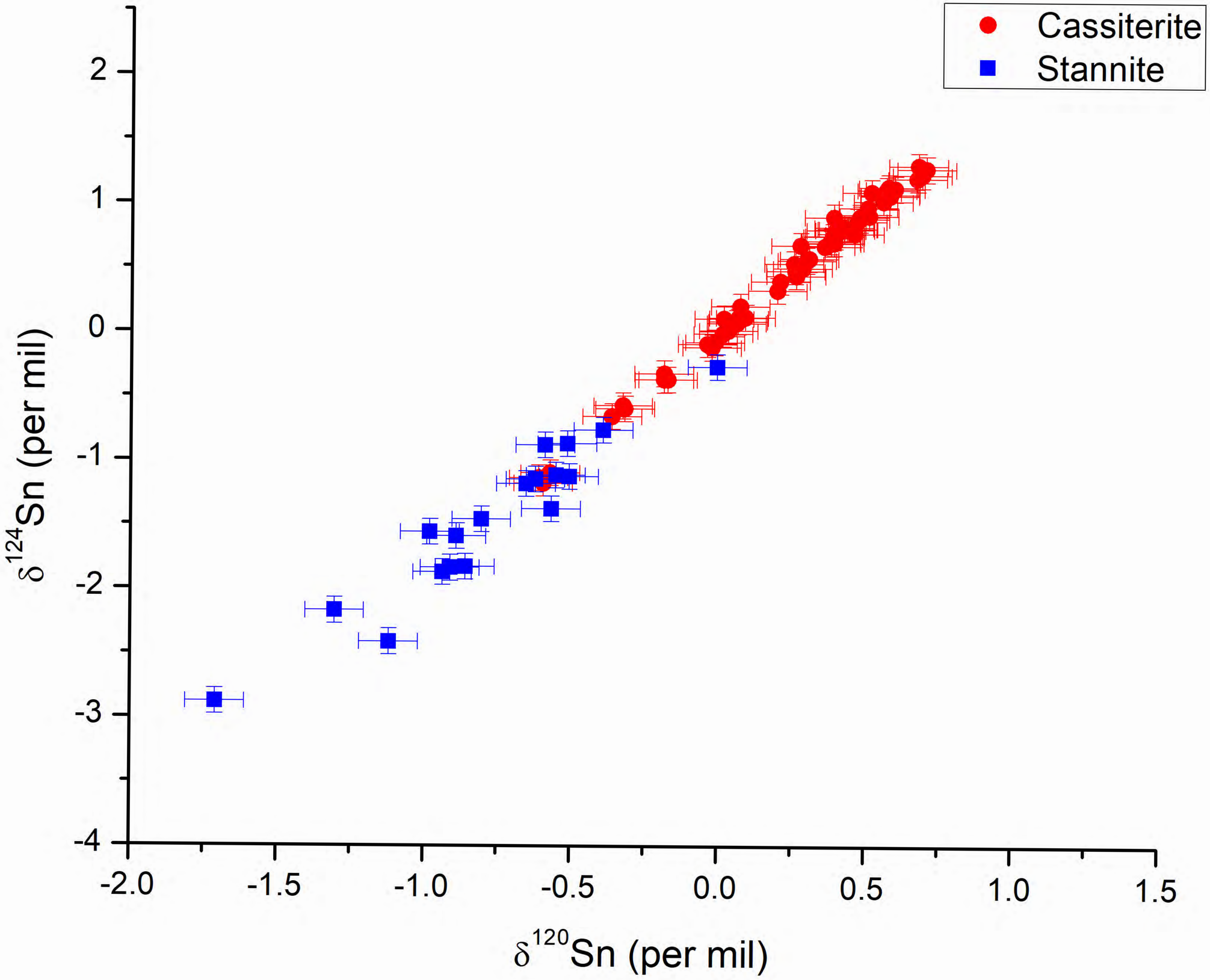
Cassiterite
Stannite
2
1
0
-1
-2
-3
-4
-2.0
-1.5
-1.0
-0.5
0.0
0.5
1.0
1.5
δ124Sn (per mil)
δ120Sn (per mil)

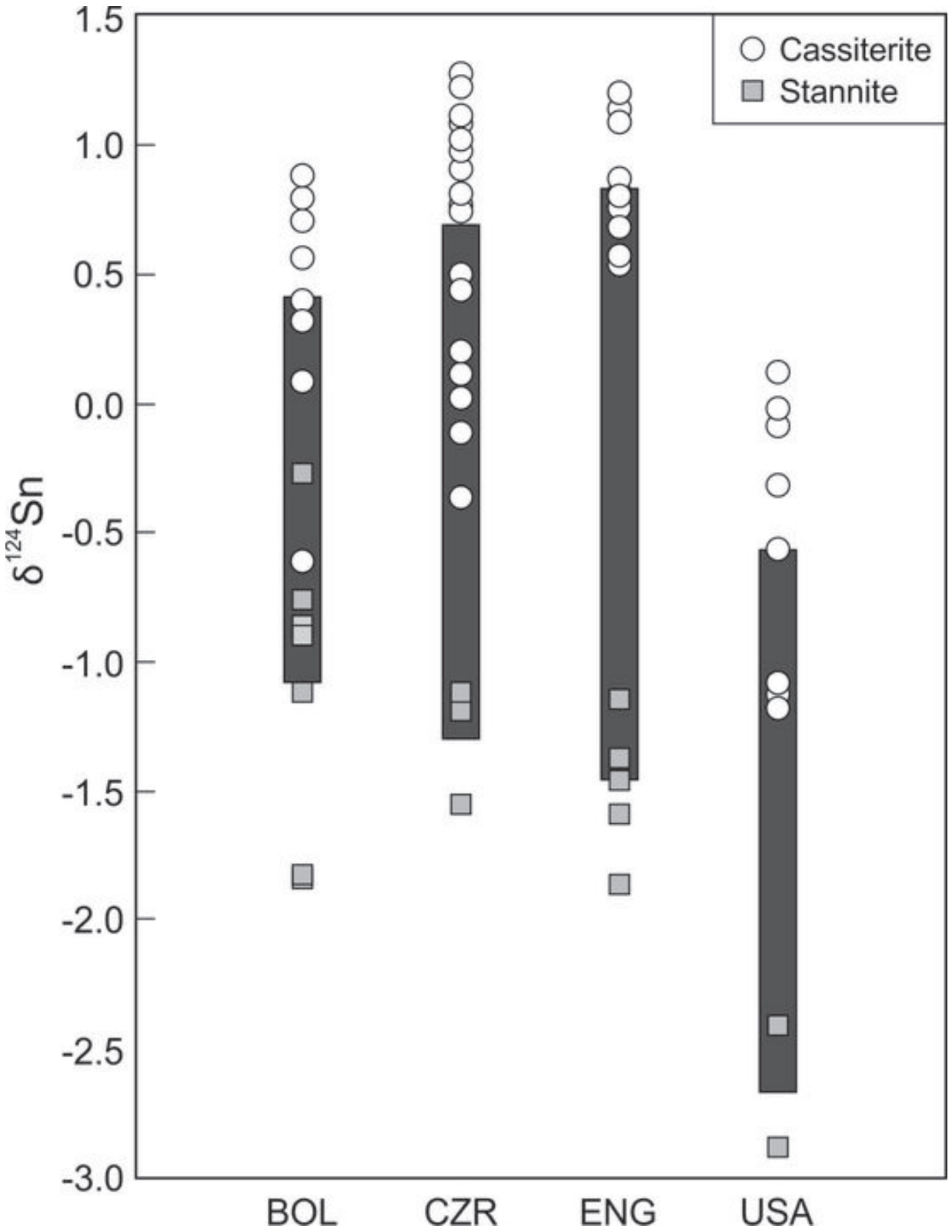
Cassiterite
Stannite
1.5
1.0
0.5
0.0
-0.5
-1.0
-1.5
-2.0
-2.5
-3.0
δ124Sn
BOL
CZR
ENG
USA

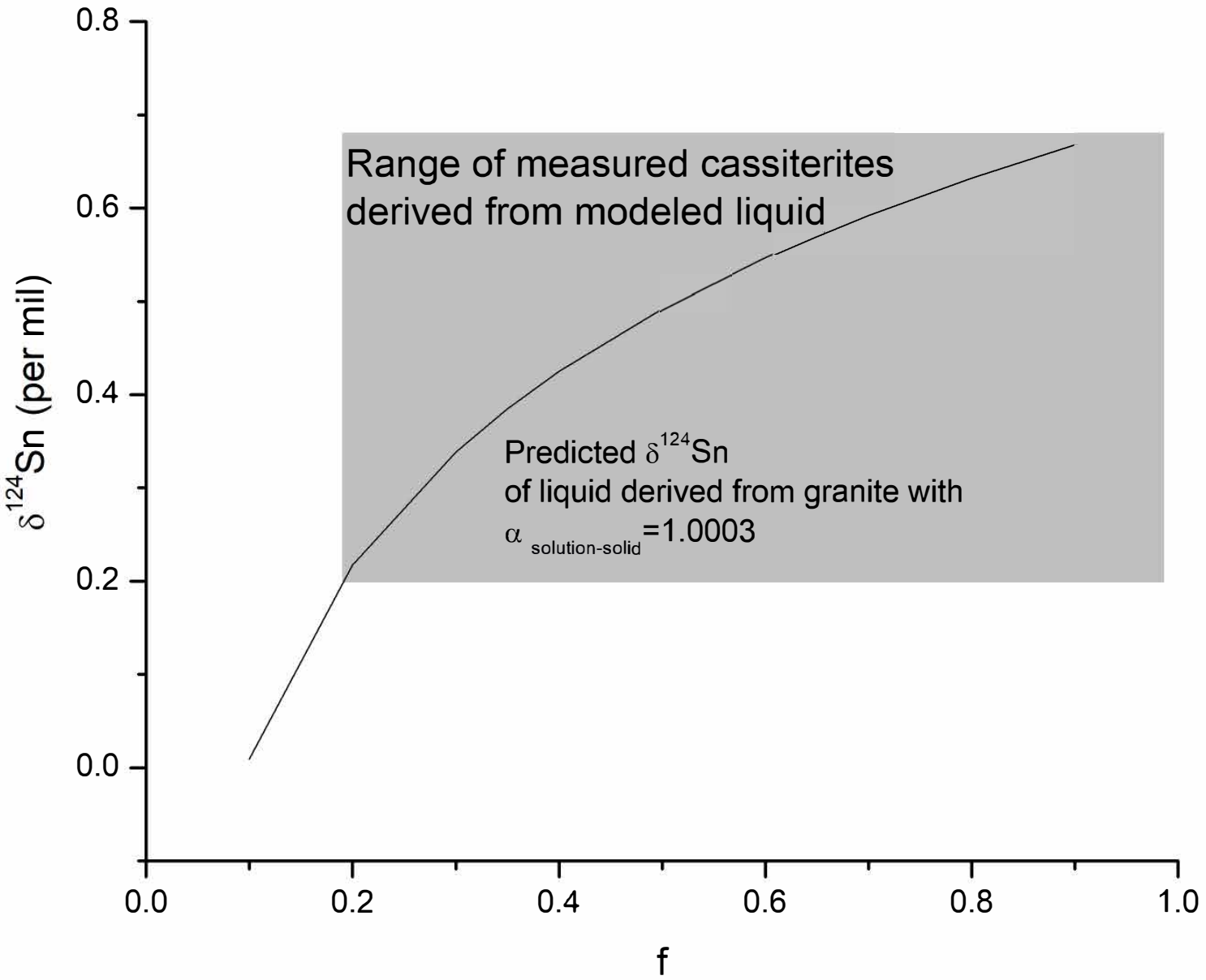
Range of measured cassiterites
derived from modeled liquid
Predicted δ124Sn
of liquid derived from granite with
α solution-solid=1.0003
δ124Sn (per mil)
0.8
0.6
0.4
0.2
0.0
0.0
0.2
0.4
0.6
0.8
1.0
f